Materials Advances

ROYAL SOCIETY OF CHEMISTRY

PAPER

View Article Online
View Journal | View Issue

Cite this: *Mater. Adv.*, 2025, 6, 7847

DLS-based optimization of ZnS–CoS nanoparticles with enhanced energy and power density for supercapacitor applications and its validation by AI models

Hafeez Ur Rehman,[a] Hamza Khan,[a] Zeeshan Abbasi,[ab] Lotfi Ben Tahar,[c] Rafaqat Ali Khan,[a] Amir Waseem[d] and Ahson Jabbar Shaikh*[a]

Zinc cobalt sulfide (ZnS–CoS) nanoparticles have emerged as promising electrode materials for supercapacitors due to their excellent electrochemical properties. However, achieving both high energy density and power density remains a challenge due to particle agglomeration and instability. In this work, dynamic light scattering-based optimization of ZnS–CoS nanoparticles is carried out by adjusting synthetic parameters including temperature, pH, reagent addition rate, and stabilizer concentration, resulting in significantly smaller particle sizes and improved stability. The optimized ZnS–CoS nanoparticle-based electrode exhibited an exceptional specific capacitance of 1156 F g^{-1}, an energy density of 194 Wh kg^{-1}, and a power density of 7260 W kg^{-1}, which are significantly higher than the values reported in the literature. Electrochemical impedance spectroscopy (EIS) results confirmed lower charge transfer resistance (35.88 Ω), indicating faster ion transport and enhanced conductivity. Moreover, the optimized ZnS–CoS electrode demonstrated remarkable cycling stability, retaining 93.87% capacitance after 10 000 cycles. The charge transfer mechanism was understood by computational studies and four different machine learning models, namely, stacking regressor, TPOT, ANN, and RSM models, which were applied to verify the experimental specific capacitance of ZnS. The accuracy of performance is best for the stacking regression model, followed by ANN, TPOT, and RSM models. These results highlight the critical role of nanoparticle size optimization in enhancing the electrochemical performance and demonstrate DLS-optimized ZnS–CoS as a superior candidate for next-generation supercapacitors.

Received 4th August 2025,
Accepted 8th September 2025

DOI: 10.1039/d5ma00846h

rsc.li/materials-advances

1. Introduction

The transition from fossil fuels to sustainable energy sources has intensified research on efficient energy storage technologies. Among various energy storage devices,[1,2] supercapacitors (SCs) have gained attention due to their high power density, fast charge–discharge rates, and long cycle life applications.[3–6] SCs can be considered ideal candidates for hybrid electric vehicles, reserve storage systems, defense systems, high-energy industrialization systems and for providing data security for computer and mobile phones.[7,8] Supercapacitors are often hindered by low energy density, necessitating the development of advanced electrode materials.[5,9]

Transition metal sulfides (TMSs) have emerged as promising candidates for SC electrodes due to their low cost, high electrical conductivity, multiple oxidation states, superior redox activity, and excellent specific capacitance.[10–14] Among TMSs, zinc sulfides and cobalt sulfides stand out due to their high theoretical capacitance, cost-effectiveness, and eco-friendly nature.[15–17] However, pure ZnS and CoS suffer from poor specific capacitance and significant agglomeration.[18,19] To address this challenge, mixed ZnS–CoS nanoparticles have been explored, leveraging the synergistic effect of Zn and Co to enhance the electrical conductivity, stability, and electrochemical performance.[20] The combination of Zn and Co in a sulfide matrix enhances the electrochemical activity, conductivity, and cycling stability, making ZnS–CoS highly efficient for energy storage applications. ZnS–CoS offers a balance between high specific capacitance and good electrical conductivity while outperforming many metal oxides and carbon-based materials in energy density.

[a] *Department of Chemistry, COMSATS University, Islamabad – Abbottabad Campus, Abbottabad-22060, KPK, Pakistan. E-mail: ahson@cuiatd.edu.pk, ahsonjabbar@hotmail.com; Tel: +92-(0)334-377-0104*
[b] *National Synchrotron Radiation Laboratory, University of Science and Technology of China, Hefei, Anhui-230029, China*
[c] *Department of Chemistry, College of Science, Northern Border University, P.O. Box 1231, Arar-91431, Saudi Arabia*
[d] *Department of Chemistry, Quaid-i-Azam University Islamabad, Islamabad-45320, Pakistan*

Synthesis methods are important tools for determining the final structure and characteristics of the resulting materials. To date, various methods including precipitation[6,21–23] hydro/solvothermal processes,[24] electrodeposition[25] and self-template processes[25] have been reported for the synthesis of pure and mixed TMSs. Due to the ease of handling, scalability, uniform mixing at the nano level, and control of particle size and shape, precipitation is considered as an effective method for the synthesis of nanoparticles.[26–28]

Although extensive work has been done on mixed metal sulfide nanoparticles, very limited work has been done for controlling the size and stability of mixed transition metal sulfide nanoparticles. The optimization of nanoparticles involves the systematic adjustment of various parameters to enhance their properties and performance for specific use. The parameters that can be altered are the concentration of constituent sulfides, pH, temperature, reagent addition rate, stabilizer concentration, *etc.*[29,30] This results in control of size, shape, composition, and surface chemistry of the resulting nanoparticles. Furthermore, the interactions between nanoparticles and their surroundings can be analyzed to better understand the impact of their performance.[31,32]

In the last few decades, machine learning approaches have been broadly used in materials science to support the discovery of new materials and predict their performance with accuracy.[33] Machine learning technology accelerates the development and analysis of energy materials, improves accuracy, and reduces research time.[34] Key supercapacitor performance metrics including specific capacitance,[35] power density, energy density,[36] and remaining useful life[37] can be predicted using machine learning models. Both modeling-based forecasting techniques and data-driven methodologies can be used to produce these predictions, leading to more precise performance evaluation and productive material optimization.

We believe that particle size and morphology control[38] is an effective strategy for improving the electrochemical performance of TMS-based electrode materials. Over the years, significant efforts have been devoted to exploring the applications of TMSs as electrode materials. However, to the best of our knowledge, no strategies have been defined yet to further improve the specific capacitance, power density, energy density, and other parameters of already good-performing materials. In the present study, we trained stacking regressor and TPOT machine learning models and then successfully applied them to verify the specific capacitance calculated experimentally.

Although ANN and RSM machine learning models are frequently used in the synthesis and optimization of nanoparticles, our work presents a distinct novelty because specific capacitance prediction has mostly been documented for carbon-based[39–41] and metal oxide-based nanoparticles.[42,43] To the best of our knowledge, the specific capacitance of metal sulfides has not been predicted yet. Additionally, we predicted specific capacitance at different scan rates, which are not documented in the literature. Although machine learning models are significant tools, but they face limitations such as overfitting, high computational demand, and limited interpretability.[44] In the present work, we handle these issues by using linearized data and advanced machine learning (ML) approaches to obtain accurate and robust predictions.

2. Materials and methods

Zinc acetate dihydrate ($Zn(CH_3COO)_2{\cdot}2H_2O$), sodium sulfide ($Na_2S$), cobalt acetate hexahydrate ($Co(CH_3COO)_2{\cdot}6H_2O$), and polyvinyl alcohol were used in the experiments, which were purchased from Dae-Jung Chemicals and Metals Co., Ltd, Republic of Korea. All the solvents and reagents were used exactly as supplied without further purification. First, a 0.1 M stock solution of zinc acetate and cobalt acetate was prepared. Then, a 0.2 M stock solution of sodium sulfide was prepared. After that, a 1% solution of polyvinyl alcohol was prepared by dissolving 1 g of PVA in 100 mL of distilled water and stirring at 1500 rpm for 30 minutes at 50 °C.

2.1 Synthesis of ZnS NPs

In a 50 mL conical flask, 10 mL of PVA solution and 10 mL of 0.1 M zinc acetate were added. The flask was then heated to 40 °C and stirred at 1300 rpm using a magnetic stirrer on a hot plate. Then, 20 mL of 0.2 M $Na_2S{\cdot}3H_2O$ solution was rapidly added to this solution, while the temperature was maintained at 40 °C. White precipitates were formed after 90 minutes of stirring. The resulting zinc sulfide nanoparticle solution was then centrifuged at 8000 rpm for 20 minutes. The precipitates were washed three times with distilled water and kept at 110 °C for 12 hours in an oven for complete drying.

2.2 Synthesis of CoS NPs

First, 10 mL of 0.1 M cobalt acetate solution was added to 10 mL of 1% PVA solution in a 50 mL conical flask and placed on a hot plate magnetic stirrer at 40 °C and stirred at 1300 rpm. Then, 20 mL of 0.2 M $Na_2S{\cdot}3H_2O$ solution was quickly added to this solution, while the temperature was maintained at 40 °C with constant stirring. After 90 minutes of stirring, black precipitates of cobalt sulfide were observed. After centrifuging the prepared solution at 8000 rpm, the precipitates were washed three times with distilled water and placed in an oven at 110 °C for drying.

2.3 Synthesis of ZnS–CoS nanoparticles

ZnS–CoS (50 : 50) mixed metal sulfide nanoparticles were synthesized *via* the simplest co-precipitation process. A conical flask containing 10 mL of PVA solution and 5 mL of each 0.1 M zinc acetate and cobalt acetate solution was placed on a hot plate magnetic stirrer at 40 °C and stirred at 1300 rpm. Then, 20 mL of 0.2 M $Na_2S{\cdot}3H_2O$ solution was quickly added to this mixture, while the temperature was maintained at 40 °C with constant stirring at 1300 rpm. After 90 minutes, a black solution of mixed cobalt sulfide and zinc sulfide was produced. The prepared solution was centrifuged, washed three times with distilled water and then kept in an oven at 110 °C for further drying.

2.4 Concentration-dependent synthesis of ZnS–CoS nanoparticles

The co-precipitation method discussed above was used to synthesize three different kinds of mixed ZnS–CoS nanoparticles, namely (25 : 75), (50 : 50), and (75 : 25), using different amounts of zinc acetate and cobalt acetate, *i.e.*, 2.5 mL : 7.5 mL, 5 mL : 5 mL, and 7.5 mL : 2.5 mL, respectively. Depending on the stability, polydispersity index, particle size, and optical properties, further optimization was carried out on 50 : 50 mixed metal sulfide nanoparticles.

2.5 Temperature-dependent synthesis of ZnS–CoS nanoparticles

The above-mentioned method was used for synthesizing mixed ZnS–CoS nanoparticles at different temperatures (20 °C, 40 °C, 60 °C, and 80 °C). Hydrodynamic size, PDI, and stability are all greatly affected by temperature. Based on the results, further optimization was carried out at 80 °C.

2.6 pH-Dependent synthesis of ZnS–CoS nanoparticles

First, the pH of the solution containing 1% PVA (10 mL), 0.2 M $Na_2S{\cdot}3H_2O$ (20 mL), and 0.1 M zinc and cobalt acetate solution (5 mL + 5 mL) was determined to be 11.5. The pH levels of 3, 5, 7, 9, 11, and 13 were adjusted by adding 0.1 M HCl or NaOH while maintaining the ideal temperature of 80 °C and keeping 1 : 1 ratio of metal salts. The synthesis procedure was followed as mentioned above. Based on the smaller size and reasonable stability, further improvements were made at pH 7.

2.7 Reagent rate-dependent synthesis of ZnS–CoS nanoparticles at room temperature

Under the ideal condition of 1 : 1 ratio of salts, 80 °C, and pH 7, the effect of the sulfide source ($Na_2S{\cdot}3H_2O$) addition rate on mixed metal sulfide nanoparticles was investigated. Using the above procedure, sodium sulfide was added rapidly, and slow additions over time period of 5, 10, 15, and 20 minutes respectively, with the best results obtained from rapid addition of the sulfide source.

2.8 Stabilizer-dependent synthesis of mixed ZnS–CoS nanoparticles

The capping agent acts as a stabilizing and size-controlling component. The procedure described above was followed to synthesize mixed metal sulfide nanoparticles without PVA and with varying amounts of PVA concentrations of 0.5%, 1%, and 2% under optimized conditions such 1 : 1 ratio of salts, pH 7, 80 °C, and quick addition of reagent. The optimal concentration of PVA was found to be 2%.

2.9 Electrode fabrication

Active material, carbon black (or graphite), and Nafion were mixed in a weight ratio of 8/1/1. All of the materials were combined using a pestle and mortar, and a thick slurry was obtained by adding 10% Nafion drop by drop. An Ni foam was used as the substrate for the electrode fabrication process; the Ni foam was weighed before electrode material deposition, and the electrode material was then transferred onto the Ni foam, so that a uniform layer was formed. After that the nickel foam was dried in a vacuum oven at 60 °C. The active mass of the electrode deposited on the Ni foam was calculated by the weight difference between the electrodes before and after deposition and drying.

2.10 Electrochemical studies

ZIVE SP1 was used for various electrochemical analyses including CV, GCD, and EIS. In this study, 1 M KOH was used as an electrolyte. A Pt wire and silver/silver chloride electrodes were used as counter and reference electrodes, respectively, while a nickel foam was used as the working electrode. CV and GCD experiments were conducted in the potential window of −0.4 to 0.6 V. An EIS experiment was conducted in the frequency range of 0.01 Hz to 100 kHz.

Specific capacitance was calculated from the CV curve using the following equation:

$$C_p = A/(2m\nu dV) \quad (1)$$

where C_p is the specific capacitance, A is the integrated area, m is the mass of electrode materials, ν is the scan rate, and dV is the difference in the potential window. The window potential is generally measured in volts.[45,46]

The following equation was used to calculate the specific capacitance from the GCD curve:

$$C_s = I_m \times \Delta t/\Delta V \quad (2)$$

where ΔV stands for the potential window. Δt is the discharge time while I_m is the current density. Energy density E and power density P were determined using the following equation:

$$E = C_s \times \Delta V/7.2 \quad (3)$$

$$P = 3600 \times E/\Delta t \quad (4)$$

2.11 Machine learning model development

All machine learning model development, training, and evaluation were conducted using the Python programming language (version 3.9). The neural network models were implemented using the TensorFlow library (version 2.x), with Keras APIs for model construction and training. Data preprocessing tasks, such as feature scaling and train-test splitting, were performed using scikit-learn (version 0.24), specifically employing the StandardScaler, train_test_split, and performance metric functions such as mean squared error (MSE) and R^2 score. The visualization of model performance (scatter plots of actual *vs.* predicted values) was performed using Matplotlib (version 3.4). Tabular data manipulation and input data reading from Excel files were handled using pandas (version 1.3). The experimental data were imported from a Microsoft Excel (XLSX) file. Each scan rate dataset was trained using an independent feed-forward neural network (ANN) consisting of two hidden layers (64 neurons each, ReLU activation), and a single output neuron for regression. Models were compiled using the Adam optimizer

and the mean squared error (MSE) loss function. Model training was performed over 100 epochs with a batch size of 16.

In this study, feed-forward artificial neural networks (ANNs) that are well established for regression problems involving complex non-linear relationships between input variables and the target output were used. Operating parameters such as scan rate have a significant impact on the specific capacitance of electrochemical materials, and feed-forward ANNs are the best choice to learn these non-linear dependencies compared to conventional linear models. Two hidden layers were chosen to maintain a balance between computational simplicity and predictive accuracy. Our initial trials revealed that one hidden layer was not sufficient to fully capture the non-linear response, and that more than two layers increased the risk of overfitting. A total of 64 neurons were assigned to each hidden layer, which provides sufficient function approximation capacity while maintaining a manageable model complexity. This design choice aligns with material modeling, which is used for small-to-medium networks to avoid overparameterization when working with small experimental datasets.

The hidden layers use the ReLU activation function, which is commonly known as the default activation, is computationally efficient, and avoids vanishing gradient issues used in modern ANN applications. Since specific capacitance is a continuous-valued property and the task is a regression problem, a single linear output neuron was used. The Adam optimizer, a popular algorithm that adaptively modifies learning rates and generally ensures faster convergence than conventional stochastic gradient descent, was used to train the model. Since the mean squared error (MSE) loss function is the default option for regression models and assesses larger deviations more significantly, it was selected to accurately predict capacitance values.

Training was carried out with a batch size of 16 over 100 epochs. These values were selected after initial testing, which demonstrated that this configuration offered a favorable trade-off between convergence speed, training stability, and computational efficiency. For this relatively small dataset, smaller batch sizes give more stable weight updates, but a greater number of epochs did not significantly improve validation metrics. The scan rate was selected as the input feature because it is a physically valuable predictor and has a strong correlation with specific capacitance, as observed in experiments. To ensure that all values were on a similar scale and to enhance numerical stability during optimization, the data were standardized using scikit-learn's StandardScaler before training. By examining the trained ANN models using mean squared error and coefficient of determination (R^2), the accuracy of these parameters was verified. Both metrics indicated that the network architecture and training parameters were suitable for predicting the specific capacitance of ZnS nanoparticles.

3. Characterization

3.1 UV-visible absorption spectroscopy

A double-beam SPECORD 200+ spectrophotometer purchased from Analytik Jena, Germany, having a wavelength range of 190–1100 nm and equipped with a deuterium and halogen lamp was used for performing UV-visible absorption spectroscopy. First, 1 mg of material was dissolved in 15 mL of water, and the mixture was sonicated for 20 minutes at 40 °C. Then, 1 mL of solution was diluted to 10 mL with distilled water, and the solution was again sonicated for 10 minutes at 40 °C. The analysis was performed in a quartz cuvette with a path length of 10 mm.

3.2 Dynamic light scattering

Zeta-Sizer Nano (model ZSP Malvern Analytical Technology, UK) and Malvern zeta-sizer software (v 8.02) were used to analyze ZnS, CoS, and their mixed metal sulfides at different optimization levels for hydrodynamic size, polydispersity index, and zeta potential studies. A polystyrene cuvette was used to measure the size and polydispersity of the sample. For zeta potential investigation, a disposable folded capillary cell (DTS1070) was used. The temperature was fixed at 25 °C. A 173° non-invasive backscatter mode was employed to determine the size and M3-PALS technique was used to evaluate the zeta potential.

3.3 X-ray diffraction

A Bruker D8 Advance X-ray diffractometer was used to record the sample's XRD diffraction peaks, with (Cu) Kα radiation at a wavelength of λ = 1.5406 Å and a step size of 0.013°. The generator was set at 40 mA and 45 kV, and the scan range was 2θ = 20°–90°. The X'PERT 3 software was employed to compare the results with reference peaks.

3.4 FT-IR spectroscopy

A PerkinElmer device with Spectrum IR software version 10.62 was used to perform Fourier transform infrared (FTIR) spectroscopy studies of metal sulfide nanoparticles. The solid nanoparticles were reduced to powder and deposited to the ATR crystal. The attenuated total reflectance (ATR) mode was used to generate the FT-IR spectra in the wavenumber range of 500 cm^{-1} to 4000 cm^{-1}.

3.5 Scanning electron microscopy

A high-performance SEM-3100 with a magnification of 300 000× working at an accelerating voltage of 1 kV to 30 kV was used to study the surface morphology of the synthesized materials.

3.6 BET analysis

Nitrogen adsorption–desorption measurements were carried out using a Quantachrome Nova Station B instrument. Approximately 95 mg of the sample was degassed at 150 °C for 10 hours to remove surface moisture and contaminants. The analysis was conducted at 77.3 K using nitrogen gas, with an equilibration time of 50/75 seconds (adsorption/desorption).

4. Results and discussion

4.1 DLS-based optimization of nanoparticles

4.1.1 Effect of precursor concentration. ZnS, CoS, and their mixed sulfide (ZnS : CoS = 75 : 25, 50 : 50, and 25 : 75)

nanoparticles were synthesized and characterized by UV-vis spectroscopy, DLS, and zeta stability measurements. The UV-visible analysis was performed in the range of 200–800 nm for all (mixed) metal sulfide nanoparticles, and the graphs were normalized at 216 nm, as shown in Fig. 1a. The absorbance peaks of ZnS and CoS appear at 221 nm and 214 nm, respectively, which correspond to the literature values and confirm the formation of ZnS and CoS NPs.[47,48] In the case of mixed metal sulfide (50 : 50), the characteristic peaks of both ZnS and CoS are visible at 221 nm and 214 nm, respectively, which proves the synthesis of mixed metal sulfide nanoparticles. Fig. 1b describes the zeta potential of mixed ZnS–CoS nanoparticles prepared with different concentrations of salts. It is clear that the stability of mixed metal sulfides is less than that of pure metal sulfides except for 50 : 50, which is close to the stability of pure ZnS. Among all, pure cobalt sulfide nanoparticles are most stable followed by pure ZnS. The zeta potential values can be influenced by many factors such as pH, ionic strength, concentration of different components, and specific conditions used.[48] The hydrodynamic backscattered particle size of different ratios of metal sulfides is shown in Fig. 1c, where the hydrodynamic backscattered size of pure ZnS

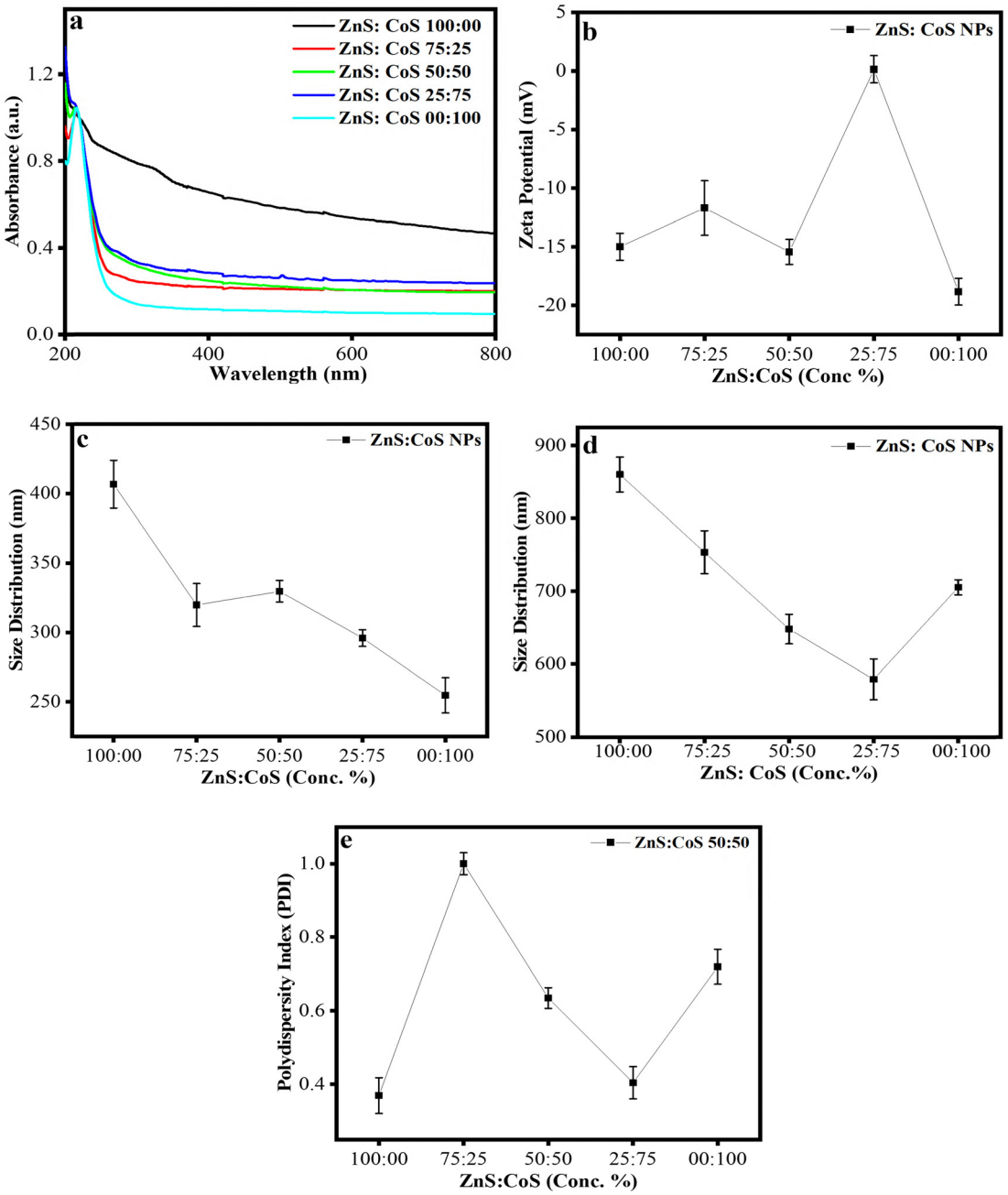

Fig. 1 Characterization of mixed ZnS–CoS nanoparticles prepared at different concentration ratios: (a) UV-vis absorption spectra, (b) zeta potential, (c) hydrodynamic size (backscattered), (d) hydrodynamic size (forward scattered), and (e) polydispersity index (PDI).

and CoS was found to be 406 nm and 245 nm, respectively. It is clear that the hydrodynamic backscattered size gradually decreases with the increase in the concentration of cobalt sulfide. The same trend was observed for the forward scattering angle except for cobalt sulfide, which shows 707 nm size, as shown in Fig. 1d. Fig. 1e expresses the PDI values that have no regular trend; however, the increasing concentration of cobalt in mixed sulfides results in a lower PDI, hence better control in size.

4.1.2 Effect of temperature. The mixed sulfide (50 : 50) was chosen based on higher stability and synthesized at 20 °C, 40 °C, 60 °C, and 80 °C. Fig. S3a shows the UV-vis spectra of mixed ZnS and CoS nanoparticles prepared at these different temperatures. The graphs are normalized at 212 nm. The characteristic peaks as observed previously are also observed here; however, no significant difference is observed in the UV-vis peaks. Fig. S3b represents the zeta potential values of nanoparticles synthesized at these temperatures. It is clear that with the increase in temperature, there is a substantial decrease (negatively) in the zeta potential values, representing higher stability, hence mixed nanoparticles are more stable when synthesized at 80 °C. Fig. S3c and d depict the backscatter and forward scatter hydrodynamic size distribution of the mixed ZnS–CoS nanoparticles synthesized at these temperatures. It is observed that backscattered size distribution decreases with the enhancement in the temperature that corresponds with the literature,[29] as the reaction is relatively slow at lower temperatures causing the particles to grow and agglomerate, whereas faster kinetics play an important role at higher temperatures, causing smaller and uniform size of nanoparticles.[49] Backscattering is sensitive to smaller particles, while larger particles prefer to be scattered in a forward direction;[29] therefore, when the size is measured at the forward angle, it is always larger and generally a reversed sequence is observed as compared to the size measured at the backscatter angle. As a result, forward scattering shows an increase in size with the increase in temperature. Overall, better control of size is observed at 80 °C. The polydispersity index of mixed ZnS–CoS nanoparticles at these temperatures is shown in Fig. S3e, where it is clearly observed that polydispersity continuously decreases as the temperature increases, with the lowest polydispersity observed at 60 °C, and after that, there is a slight increase in polydispersity at 80 °C. Hence, with the increase in the synthesis temperature of mixed metal sulfide nanoparticles, there is a shift from broad size distribution to uniform size distribution, and the best uniform size distribution is observed at 60 °C.

4.1.3 Effect of pH. We chose 80 °C as an optimal temperature based on the higher stability and uniform small size of nanoparticles. The effect of pH was studied, where different pH values were maintained, *i.e.* 3, 5, 7, 9, 11, 12, and 13. The UV-vis graphs of the resulting nanoparticles are shown in Fig. S4a, which are normalized at a wavelength of 212 nm. Fig. S4b shows the zeta potential values of these mixed ZnS–CoS nanoparticles synthesized at different pH values. Although there is no regular trend of zeta potential values, better stability can be observed at higher pH values, *i.e.*, at pH = 11 and 13, as the zeta potential decreases.

The backscatter hydrodynamic size of mixed metal sulfides prepared at different pH values is shown in Fig. S4c. The hydrodynamic radius (R_{hyd}) decreases first at pH 5, and then steadily increases in size with the increase in pH till pH 11, after which again there is a decreasing trend in size. The hydrodynamic size at pH 13 is observed to be 262 nm. Therefore, a general trend could be explained, as a higher pH value causes more stability and relatively smaller size, hence potential agglomeration is prevented at higher pH values. Fig. S4d shows the forward scatter hydrodynamic size of the mixed sulfide nanoparticles. There is no regular trend of forward scatter hydrodynamic size, but with the variation in pH, a minimum size is observed at pH 5. Fig. S4e depicts the polydispersity index of mixed sulfide nanoparticles synthesized at different pH values, where we do not find any regular trend of polydispersity index with the variation in the pH values. The highest polydispersity index (0.93) is observed at acidic pH 3, while the lowest PdI value (0.33) is observed at neutral pH. It means that at neutral pH, uniform size distribution of particles occurs.

4.1.4 Effect of the addition of sulfide source. ZnS–CoS were synthesized at different times of addition of sulfide source (Na_2S) after the reaction started, *i.e.*, quick addition, 5-minute addition, 10-minute addition, and 20-minute addition. Ideal pH 7 and temperature at 80 °C were maintained for the 50/50 ratio of ZnS : CoS. The UV-visible spectra displayed in Fig. S5a shows no significant difference. Fig. S5b shows the zeta potential of the synthesized mixed ZnS–CoS nanoparticles prepared at different times of addition of sulfide source. We can see that 5 minute addition has more negative values (−15.77 mV) with higher repulsion between the charged particles that prevents them from agglomeration,[50] hence higher stability. Fig. S5c shows the hydrodynamic backscattered size of mixed ZnS–CoS nanoparticles synthesized at different times of addition of sulfide source. The back scattered hydrodynamic size increased with the increase in the time of addition till 10 minutes, and then a decrease in R_{hyd} was observed at 20 minutes of addition. The best control of size is depicted for quick addition followed by 5-minute addition. Fig. S5d shows the forward scattered hydrodynamic size. An increase in R_{hyd} is observed for 5 minutes, then a decrease for 10 minutes, and again increase for 20 minutes of addition. Fig. S5e shows that the polydispersity indexes of mixed metal sulfide nanoparticles synthesized at different times of addition of sulfide source are lowest at quick and 20-minute addition and highest at 5- and 10-minute addition. Overall, the size and PdI analyses show that the best reaction kinetics occur at quick addition, yielding the lowest size and PDI value.

4.1.5 Effect of PVA ratios. Mixed ZnS–CoS nanoparticles were also optimized for different concentrations of PVA, *i.e.*, 0%, 0.5%, 1%, and 2%, after maintaining the ideal conditions, *i.e.*, 50 : 50 ratio, pH 7, 80 °C, and quick addition of sodium sulfide solution. The UV-visible spectra are shown in Fig. S6a.

Fig. S6b depicts the zeta potential of mixed metal sulfides synthesized with different concentrations of PVA. A steady decrease (negatively) in zeta potential is observed with the increase in the concentration of stabilizer. At 2% PVA

concentration, the zeta potential is more negative, *i.e.* −17 mV. Hence, decreasing the zeta potential values with the increase in stabilizer concentration indicates that stability increases by increasing the stabilizer concentration. This is because stabilizers cap the nanoparticle's surface and prevent it from agglomeration.[51] In this way, mixed sulfide nanoparticles are highly stabilized by the addition of a capping agent. Fig. S6c demonstrates the backscattered hydrodynamic size of mixed metal sulfides synthesized with different concentrations of PVA. The backscattered hydrodynamic size steadily decreases with the increase in the amount of PVA. For a maximum 2% concentration of stabilizer, a minimum size of 214 nm is achieved. Adding a higher concentration of stabilizer prevents nanoparticles from agglomeration and leads to a reduction in the size of nanoparticles.[52] Fig. S6d demonstrates the forward scattered hydrodynamic size of the mixed metal sulfides. It is obvious that R_{hyd} decreases with the increase in the concentration of PVA, and with 2% PVA concentration, the size is only 185 nm. The polydispersity of mixed sulfide nanoparticles is shown in Fig. S6e. The PDI of mixed sulfide nanoparticles synthesized without any stabilizer is lowest at 0.22, whereas an increase in the percentage of stabilizers (PVA) leads to an increase in the PDI value, reaching a maximum of 0.53 at 2%.

As a result of these investigations, large-scale synthesis was performed for 50 : 50 ratios, pH 7, 80 °C, quick addition of sodium sulfide solution, and 2% concentration of PVA. The optimized nanoparticles were further characterized and utilized for electrochemical studies.

4.2 Characterizations

4.2.1 FTIR spectroscopy analysis. Fig. 2a depicts the FTIR spectra of ZnS NPs. The bands positioned at around 2855 cm^{-1} are due to the C–H stretching vibrations of PVA.[52] The peaks appearing at 796 and 508 cm^{-1} are ascribed to the Zn–S vibrations and are characteristic of cubic ZnS.[53] The broader peak at 3366 cm^{-1} corresponds to the stretching frequency of the –OH group of PVA.[54] The absorption band at 1626 cm^{-1} is due to the C–C stretching vibrations.[55] The peak that appeared at 1135 cm^{-1} is assigned to the C–C and C–O–C bond vibration.[56] Fig. 2b depicts the FTIR spectra of CoS. The peaks appearing at 3202 cm^{-1} and 1068 cm^{-1} correspond to the O–H stretching and C–O stretching, respectively.[54] The peak positioned at 1670 cm^{-1} represents the bending of water molecules adsorbed on the surface of cobalt sulfide.[57] Fig. 2c presents the FTIR spectra of the optimized ZnS–CoS mixed metal sulfides. The peak at 1605 cm^{-1} is attributed to water molecules. The peak appearing at 607 cm^{-1} is related to the metal sulfide group.[58]

4.2.2 XRD analysis. Using a Cu anode as the radiation source, a Bruker D8 Advance diffractometer was used to study the crystalline structure of pure and mixed (50 : 50) metal sulfide nanoparticles by X-ray diffraction (XRD). The 2θ values in the XRD spectra correspond to angles at which the crystal lattice deflects X-rays. Each peak indicates a distinct set of crystal planes. The compound's crystallinity and crystallite size can be determined by these peaks. The crystalline structure of ZnS NPs was determined by analyzing their diffraction pattern, as shown in Fig. 3a, which indicates phase purity. Three significant peaks are observed at 2θ = 28.08°, 47.66°, and 56.85° assigned to the 111, 220, and 311 planes, respectively. All the crystallite peaks have solid alignment with standard JCPDS card no #01-080-0020, which verifies the blende cubic phase of ZnS nanoparticles.[43] Fig. 3b shows the XRD pattern of cobalt sulfide nanoparticles. Prominent peaks at 2θ = 29.91°, 36.62°, 47.32°, and 52.29° corresponding to the 100, 101, 102, and 110 lattice planes, respectively, are observed to have strong agreement with the JCPDS card no #65-3418 that validates hexagonal CoS.[58] Fig. 3c depicts the XRD pattern of ZnS–CoS, with the characteristic peak at 2θ = 56.85° confirming the presence of ZnS in the optimized ZnS–CoS mixed metal sulfides, while the peaks observed at 2θ = 29.91°, 36.62°, 47.32°, and 52.29° confirm the presence of CoS in mixed metal sulfides.

4.2.3 SEM analysis. Zinc sulfide's morphological analysis was performed by scanning electron microscopy. Fig. 4a shows the SEM image of the synthesized zinc sulfide NPs at 50 000× magnification with 200 nm scale bar, which reveals its nanomorphology. Cobalt sulfide's morphological analysis is illustrated in Fig. 4b, with a rod-like morphology. Mixed ZnS–CoS (50 : 50) nanoparticles are shown in Fig. 4c with a particle-like morphology.

4.2.4 BET analysis. Nitrogen adsorption–desorption analysis was performed to evaluate the textural properties of the optimized ZnS–CoS (Fig. 5a and b). The BET surface area, calculated using the multi-point method, was found to be

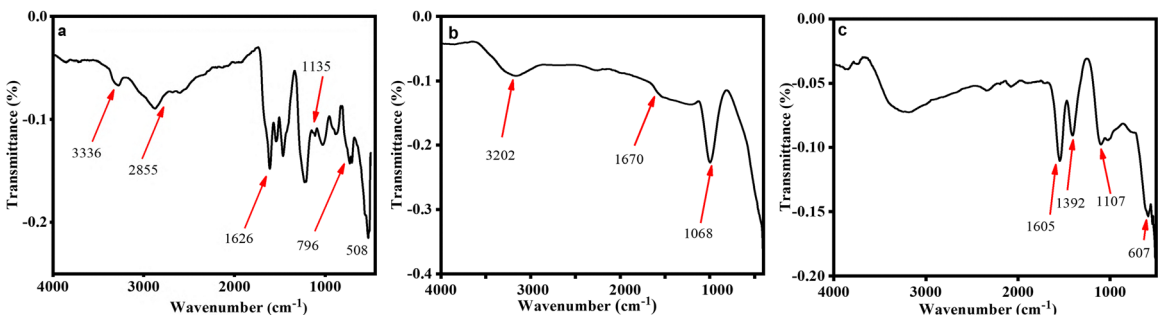

Fig. 2 FTIR spectra of (a) ZnS nanoparticles, (b) CoS nanoparticles, and (c) optimized mixed ZnS–CoS nanoparticles, showing the characteristic vibrational bands corresponding to metal–sulfur stretching and surface functional groups.

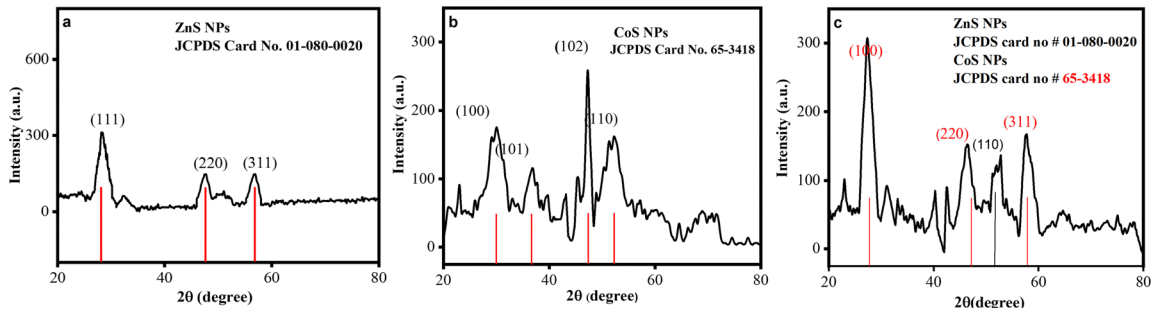

Fig. 3 XRD patterns of (a) ZnS nanoparticles, (b) CoS nanoparticles, and (c) optimized mixed ZnS–CoS nanoparticles, confirming the crystalline phases and structural composition of the synthesized materials.

386.5 $m^2\ g^{-1}$, while Langmuir surface area was found to be 552.1 $m^2\ g^{-1}$, which is higher than the BET surface area due to its assumption of monolayer adsorption, confirming a high surface area that supports enhanced charge accumulation. The C constant value of 72.89 suggests a strong interaction between the nitrogen adsorbate and the surface, confirming the material's affinity for gas molecules. The total pore volume, as determined by the DFT model, was 0.197 cc per g, closely matching the micropore volumes obtained from the HK (0.1899 cc per g) and SF (0.1735 cc per g) models, indicating that a significant portion of porosity arises from micropores. The average pore radius, based on DFT, was 6.159 Å (equivalent to a diameter of 1.23 nm), which falls within the microporous range (<2 nm). In contrast, the BJH method showed a much lower cumulative surface area of 10.96–13.89 $m^2\ g^{-1}$ and a smaller pore volume of ~0.028–0.029 cc per g, with a pore diameter centered around 4.66 nm (23.3 Å), revealing a minor mesoporous contribution.

4.3 Electrochemical studies

To evaluate the charge storage capacity and the capacitive response of ZnS, CoS, and optimized ZnS–CoS; cyclic voltammetry (CV), galvanostatic charge–discharge (GCD), and impedance spectroscopy (EIS) were carried out in an aqueous solution using a 3-electrode system. Cyclic voltammetry results are shown in Fig. 6a–c for ZnS, CoS, and ZnS–CoS nanoparticles, respectively, which were obtained at a scan rate of 5 mV s^{-1} to 100 mV s^{-1} with a fixed potential window of −0.4 to 0.6 V for all samples.

The specific capacitance was calculated using eqn (1) for ZnS, CoS, and optimized ZnS–CoS at different scan rates from 5 mV s^{-1} to 100 mV s^{-1} in the potential window of −0.4 to 0.6 V. Excellent results were obtained at 5 mV s^{-1} for each material. For ZnS, it is 315 F g^{-1} and for CoS, it is 199 F g^{-1}. For mixed metal sulfides, which were optimized under different conditions, extraordinary results were obtained, as presented in Fig. 6d. Specific capacitance was obtained to be 868 F g^{-1} for optimized mixed metal sulfides, which is more than four times that of CoS and nearly 3 times that of ZnS. With the increase in scan rate, there is an exponential decrease in the specific capacitance due to limited time availability among the electrode and electrolyte intercalation.[59]

The CV curve maintained at a higher scan revealed excellent stability of the electrode materials. In all samples, the peak current increases with the increase in scan rate that is associated with the redox reaction. In Fig. 6c, the large integration area of optimized ZnS–CoS is attributed to the synergetic effect of ZnS and CoS in mixed metal sulfides. From cyclic voltammetry results, the following conclusion can be drawn:

(1) The voltammogram's peaks seem to be well defined despite some broadening, particularly at higher scan rates. This broadening may indicate quasi-reversibility since it implies a deviation from perfect reversibility.

(2) At higher scan rates (100 mV s^{-1}), the anodic and cathodic peak separation appears to be greater than the ideal

Fig. 4 SEM micrographs of (a) ZnS nanoparticles, (b) CoS nanoparticles, and (c) optimized mixed ZnS–CoS nanoparticles, illustrating the surface morphology of the synthesized materials.

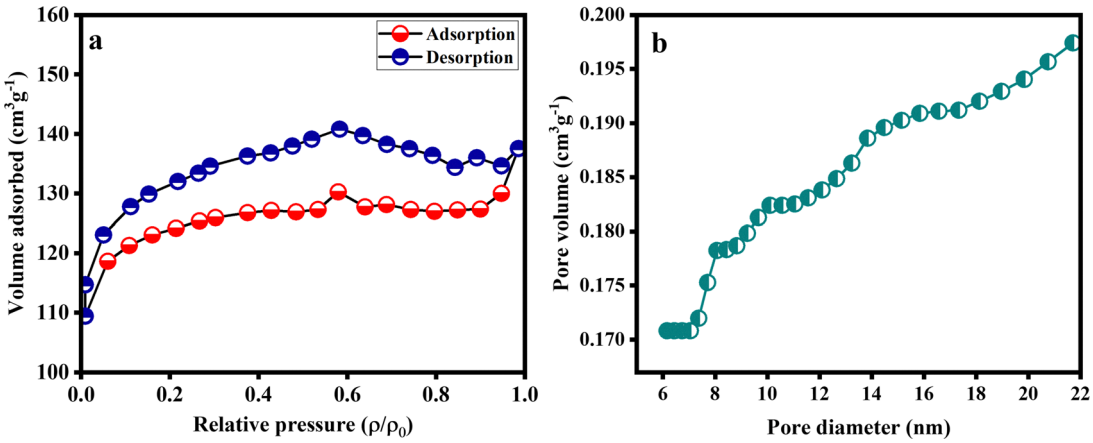

Fig. 5 (a) N_2 adsorption–desorption isotherm and (b) pore size distribution curve (derived from the BJH desorption data) of the optimized mixed ZnS–CoS nanoparticles, confirming their specific surface area and mesoporous structure.

59 mV predicted for a fully reversible process. A quasi-reversible process is characterized by increasing ΔE_p with the scan rate.

(3) Peak separation increases with the increase in scan rate (from 5 mV s^{-1} to 100 mV s^{-1}), which is characteristic of quasi-reversible reactions. The peak separation is constant for reversible processes regardless of the scan rate.

EIS was applied to achieve the kinetics of the charge transfer. Common impedance plots comprise three primary

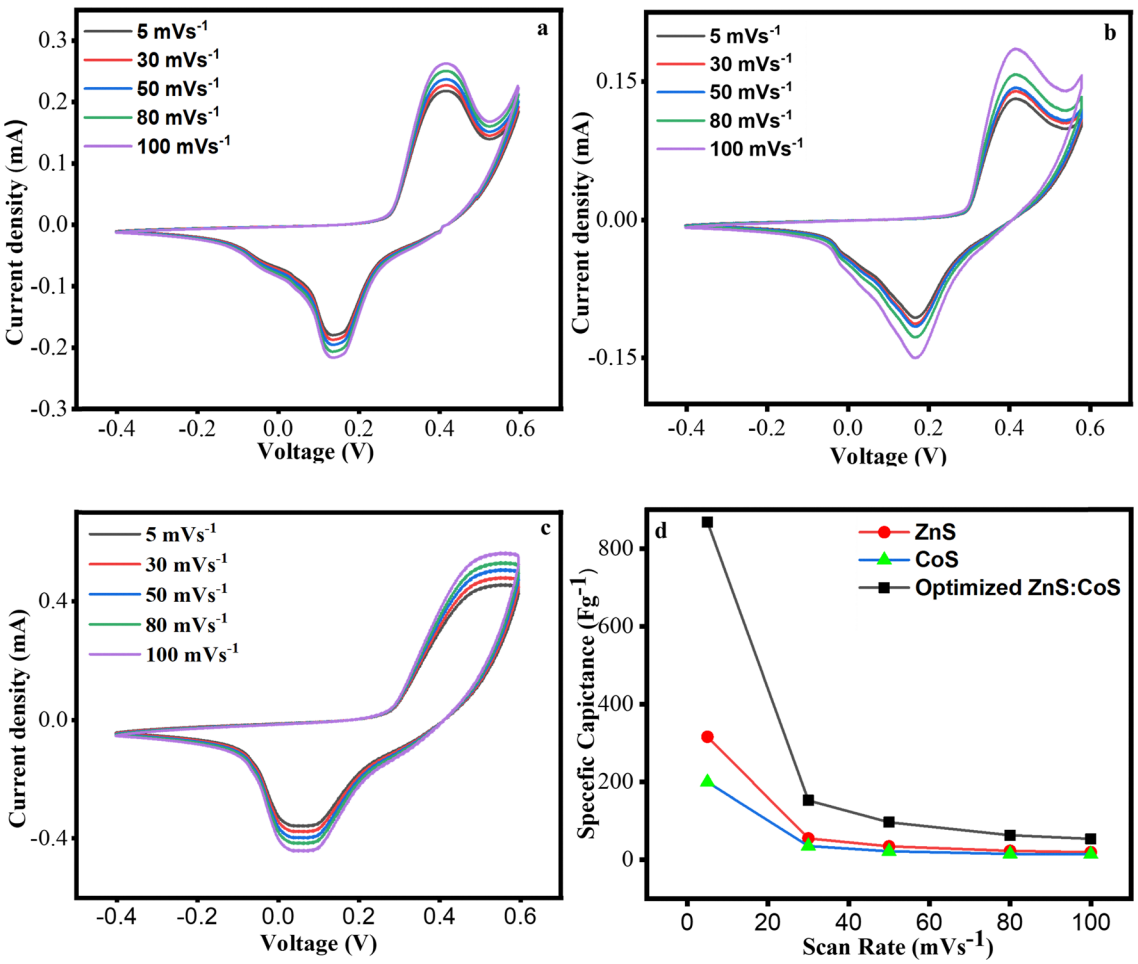

Fig. 6 Cyclic voltammetry (CV) curves recorded at different scan rates within a fixed potential window for (a) ZnS nanoparticles, (b) CoS nanoparticles, and (c) optimized mixed ZnS–CoS nanoparticles. (d) Comparative plot of specific capacitance as a function of scan rate for all the three electrodes, highlighting the superior electrochemical performance of the mixed ZnS–CoS system.

regions. A high-frequency semicircle whose diameter reflects the charge-transfer resistance (R_{ct}), a low-frequency region, and an intercept on the real axis that indicates the solution resistance. Under similar conditions, we performed electrochemical impedance spectroscopy for ZnS, CoS, and optimized ZnS–CoS, and the resulting impedance plots are illustrated in Fig. 7a. Fig. 7b shows that optimized ZnS–CoS demonstrates the lowest R_{ct} (35.88) among these three materials, as also shown in Table 1. The rapid movement of charge carriers in an electrochemical process is attributed to the synergistic effect of ZnS and CoS, which provide superior conductive support. It suggests that the maximum number of charged ions reaches the surface of the electrode to support the electrochemical redox process. Therefore, the impedance study verifies that the optimized ZnS–CoS is an outstanding material with excellent specific capacitance and superior rate performance.[60]

To assess the charge storage capacity of ZnS, CoS, and ZnS–CoS, a galvanostatic charge–discharge study was conducted at different current densities of 2, 4, 5, and 6 A g^{-1} at a fixed potential of −0.4 to 0.6, as depicted in Fig. 8a–c. The GCD curves depict the nonlinear behavior that demonstrates the faradaic reactions between the electrode materials and the electrolyte solution that has strong agreement with the CV results. The specific capacitance calculated from the GCD profile at different current densities is slightly higher than the specific capacitance calculated from CV. A decrease in the specific capacitance with the increase in current densities is observed due to the fact that electrolyte ions do not have enough time to migrate into the pores of materials.[61] It is clear from Table 2 that DLS-optimized ZnS–CoS depicts an extraordinary specific capacitance of 1156 F g^{-1} at 2 A g^{-1}, which is four times higher than that of ZnS and CoS, due to the synergetic effect of Zn and Co.

The specific capacitance of cobalt sulfide drops drastically from 130 F g^{-1} at 5 A g^{-1} to 7.44 F g^{-1} at 6 A g^{-1} (Table 2). This rapid drop is explained by slow charge-transfer kinetics and limited ion diffusion at high current densities, which significantly reduce the effective contact time between electrolyte ions and the active electrode surface.[62] Cobalt sulfide depicts a pronounced decrease in specific capacitance as the current density increases, and it is well documented in the literature. For instance, Sathiskumar *et al.* reported a specific capacitance of 348 F g^{-1} at 1 A g^{-1}. At higher current densities, this capacitance dropped significantly to 100 F g^{-1} at 20 A g^{-1}, or a 71% reduction.[63] By contrast, composites often retain specific capacitance even at high current density.[64] Additionally, our EIS results are also consistent with the specific capacitance values listed in Table 2. The significant loss in capacitance at higher current densities can be explained by the comparatively high charge-transfer resistance of cobalt sulfide (102.66 Ω). Higher surface charge resistance indicates the sluggish charge transfer kinetics that results in poor electrochemical performance.[65]

Table 1 Charge transfer resistance of pure and mixed metal sulfides

Metal sulfides	Charge transfer resistance (R_{ct}) (Ω)
ZnS	74.20
CoS	102.06
ZnS–CoS	35.88

Energy density and power density were also calculated using eqn (3) and (4) provided in the experimental section. As shown in Table 3, DLS-optimized ZnS–CoS exhibits an excellent power density of 7260 (W kg^{-1}) at an energy density of 72 (Wh kg^{-1}) at 6 A g^{-1}, which is decreased to 2420 (W kg^{-1}) at an energy density of 194 (Wh kg^{-1}) at 2 A g^{-1}, indicating a higher rate capability at a higher current density. The relation between power density and energy density is illustrated in the Ragone plot (Fig. 9a). Cycling stability is the key parameter to decide the durability and efficiency of materials. The cycling stability of optimized ZnS–CoS was determined by performing repeated charge–discharge tests at a very high current density of 20 A g^{-1} over 10 000 cycles, as expressed in Fig. 9b. Over 10 000 cycles, 93.87% capacitance is retained. Moreover, from start to end, no structural collapse and stability were observed resulting in high conductivity of DLS-optimized ZnS–CoS mixed metal sulfides. This can be confirmed by the GCD curves of first and last ten cycles, as shown in Fig. 9c and d, respectively.

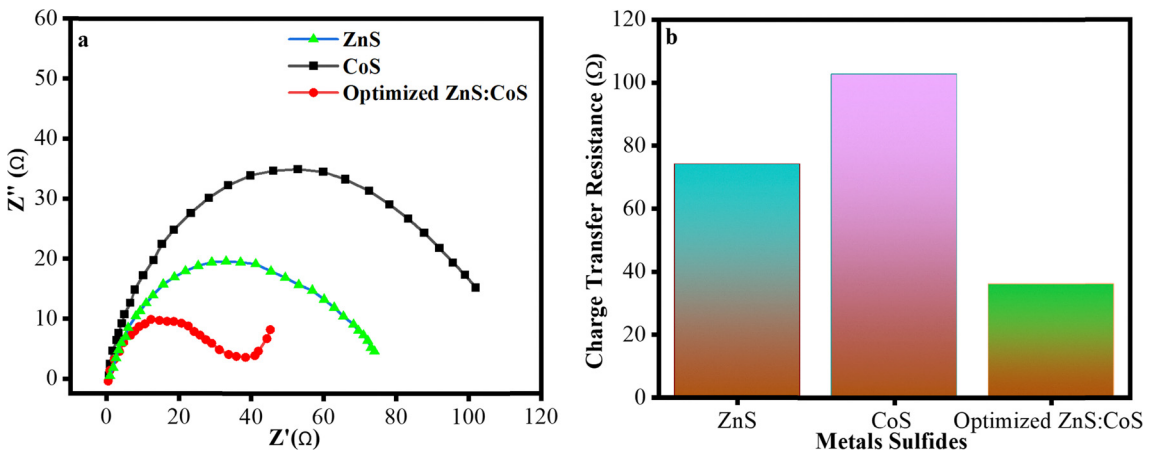

Fig. 7 (a) Nyquist plots of ZnS, CoS, and mixed ZnS–CoS electrodes, illustrating their electrochemical impedance behavior. (b) Comparative analysis of charge-transfer resistance (R_{ct}) values, demonstrating the enhanced conductivity and lower resistance of the mixed ZnS–CoS electrode.

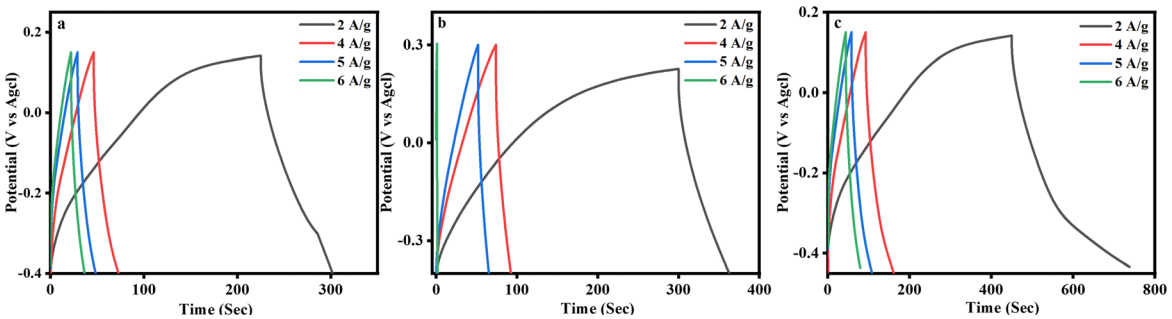

Fig. 8 Galvanostatic charge–discharge (GCD) profiles of (a) ZnS, (b) CoS, and (c) optimized ZnS–CoS electrodes recorded at different current densities, demonstrating their charge storage behavior and capacitance characteristics.

Table 2 Specific capacitance values against different current densities for ZnS, CoS, and the optimized ZnS–CoS electrode

Current densities (A g^{-1})	2	4	5	6
ZnS	264	208	190	168
CoS	248	152	130	7.44
ZnS–CoS	1156	568	540	432

To support the experimental part in qualitative manner, mathematical Dunn's model was applied. The CV curves were further investigated to explore the charge storage mechanism. For this purpose, power law equation was used to describe the relationship between the specific current and scan rate applied. The results are presented in Fig. 10.

$$i = a\nu^b \quad (5)$$

$$\log(i) = \log a + b \log \nu \quad (6)$$

In eqn (5) and (6), i, a, and b represent the current, scan rate, and constants, respectively. Using this equation, we can calculate the factor b for which the values range from 0.5 to 1. The charge storage mechanism is completely surface controlled when the value of b is close to 1. A value of b approaching 0.5 indicates a totally diffusion-controlled process. Plotting the log of a specific current against the log of scan rate in eqn (6) provides the value of factor b calculated from the slope of the straight line. As depicted in Fig. 10a, the value of b is 0.91 that is close to 1 describing that the mechanism is surface controlled. The percentage contribution can be calculated using eqn (7):

$$i(\nu) = k_1\nu + k_2\nu^{1/2} \quad (7)$$

where k_1 and k_2 indicate the constant, while $k_1\nu$ and $k_2\nu^{1/2}$ are used to describe the surface-controlled capacity and diffusion-controlled capacity, respectively. Fig. 10b represents the surface-controlled capacity of optimized ZnS–CoS, which was found to be 52.30% at 5 mV. It is clear in Fig. 10b that the diffusion-controlled contribution decreases at higher scan rates because the electrolyte ions do not have enough time to adsorb onto the electrode material. The CV curves expressing the diffusive and surface-controlled capacitance contribution of ZnS–CoS NPs by Dunn's method are shown in Fig. 10c.

Table 3 Specific capacitance, energy density, and power density at different current densities for the optimized ZnS–CoS electrode

Current density (A g^{-1})	2	4	5	6
Specific capacitance (F g^{-1})	1156	568	540	432
Energy density (Wh kg^{-1})	194	95	90	72
Power density (W kg^{-1})	2420	4840	6050	7260

In Table 4, the analysis of specific capacitance, energy density, power density, and cycling stability is presented for similar materials, as compared to our optimized ZnS–CoS mixed metal sulfide electrodes, which show a significant enhancement in energy density and power density values for our optimized material.

Zinc and cobalt mixed metal sulfides have porous structures that give large gaps and open channels, which increase the ion diffusion and charge transport and act as promising materials for supercapacitors.[72] Hydroxide ions from KOH interact with mixed metal sulfides that promote the reversible faradaic reaction.[73] The synergistic effect of zinc, cobalt, and sulfur increases the electrical conductivity, which leads to a fast and reversible charge–discharge cycle.[20] The synergistic effect also provides an enhanced surface area,[74] resulting in better charge storage. All these features make our optimized mixed metal sulfides promising materials for supercapacitor applications. The proposed mechanism for charge transfer at electrodes is shown in Scheme 1.

4.4 DFT studies

We also computationally calculated the band gaps of CoS, ZnS, and ZnS–CoS using the GAUSSIAN 09 software with a PM6 basis set (a semi-empirical method). It is a reliable method for accurately predicting the electronic properties. The calculated band gaps for ZnS, CoS, and the ZnS–CoS mixed sulfide are 2.51 eV, 2.75 eV, and 2.53 eV, respectively (Table 5). The computationally obtained HOMO–LUMO orbitals of ZnS, CoS, and ZnS–CoS NPs are shown in Fig. 11. The results indicate that by forming a structure of ZnS–CoS, the band gap is the lower side, indicating an enhancement in electronic conductivity for mixed sulfides.

The reduced band gap suggests better electron mobility for ZnS–CoS and correlates with the improved electrochemical performance and enhanced charge storage capability as

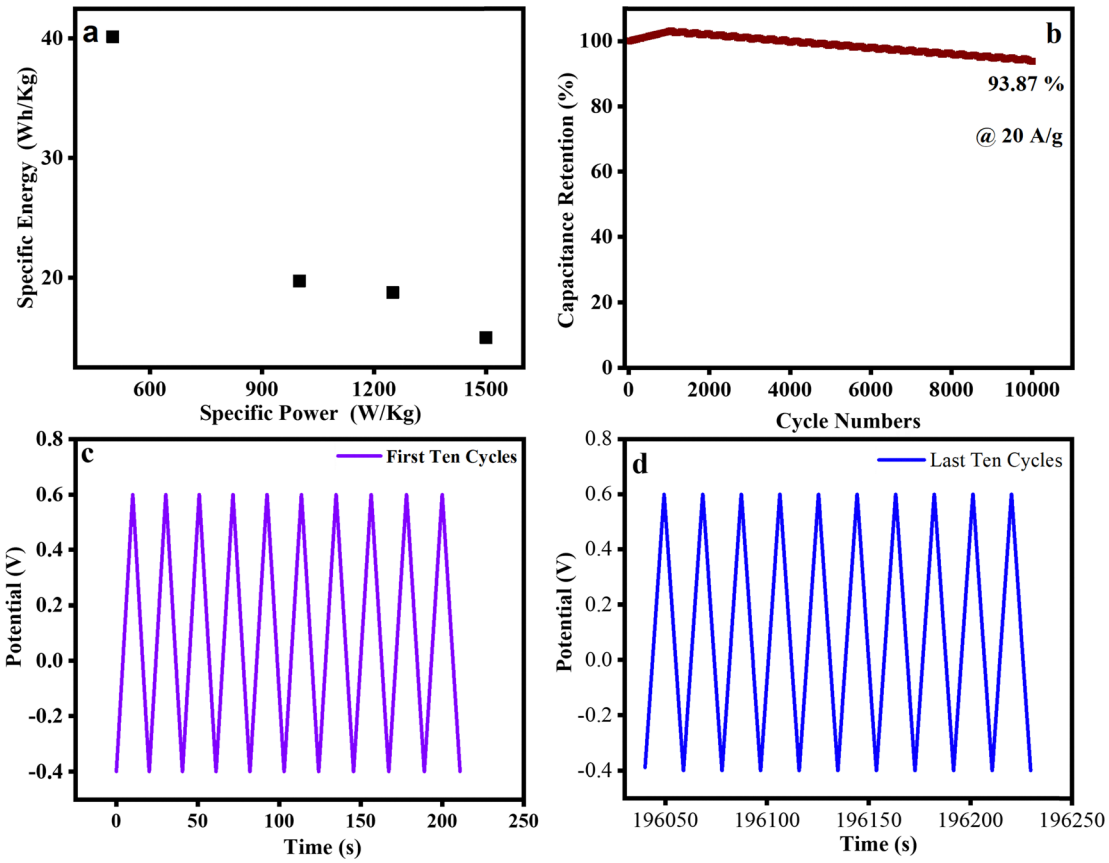

Fig. 9 (a) Ragone plot showing the relationship between energy density and power density for the optimized ZnS–CoS electrode. (b) Cycling stability performance of the optimized ZnS–CoS electrode over 10 000 charge–discharge cycles, confirming its long-term electrochemical durability. (c) GCD curves of the first ten cycles and (d) GCD curves for the last ten cycles.

observed in the experimental results. Specifically, the cyclic voltammetry (CV) analysis revealed that the specific capacitance values were 264 F g^{-1} for ZnS, 248 F g^{-1} for CoS, and significantly higher 1156 F g^{-1} for the ZnS–CoS mixed sulfide, measured at a scan rate of 2 mV s^{-1}. The results also complement electrochemical impedance spectroscopy (EIS) analysis, which demonstrated a lower charge transfer resistance for the ZnS–CoS mixed sulfide, confirming its superior electrical conductivity.

The density of states (DOS) analysis is shown in Fig. 12a–c, indicating that electron transfer between the valence and conduction bands is crucial for determining their conductivity. The Fermi level lies between these two bands, affecting the overall electron transfer mechanism. The DOS analysis provides insights into energy level formation, particularly the lowest unoccupied molecular orbital (LUMO) values. For example, in Fig. 12, the LUMO of ZnS is observed at −4.20 eV and for CoS, it is observed at −8.85 eV. When mixed sulfides are formed, *i.e.*, ZnS–CoS, the LUMO value is observed at −8.28 eV. These findings, also supported by computational and electrochemical analyses, illustrate that the synergistic effects are observed

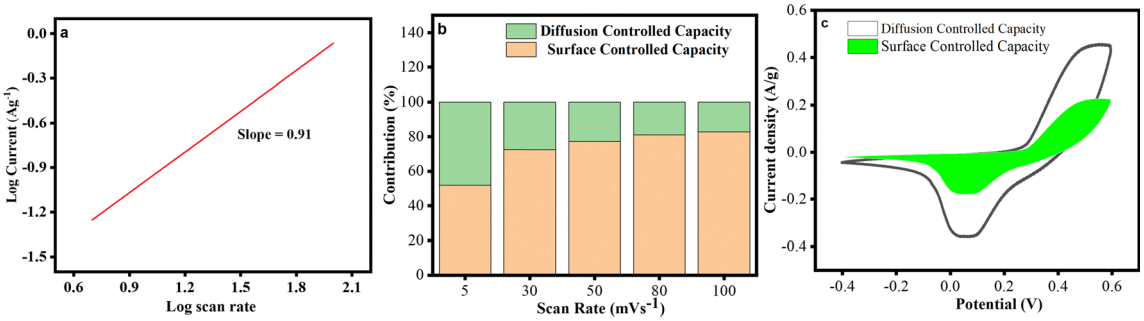

Fig. 10 (a) Linear relationship of log(i_p) *versus* log(ν) for the optimized ZnS–CoS electrode, (b) bar chart showing the relative capacitance contribution at different scan rates, and (c) CV curves analyzed using Dunn's method to distinguish the diffusive and surface-controlled capacitance contributions.

Table 4 Comparative analysis of the optimized ZnS–CoS mixed metal sulfide electrode with other literature reported electrodes

Materials	Specific capacitance (F g^{-1})	Energy density (Wh kg^{-1})	Power density (W kg^{-1})	Cyclic stability (%)	Ref.
Zn–Co–S	1269.1	45.4	805.0	91.6%	20
Multilayer dodecahedrons Zn–Co sulfide	971.01	31.63	8.09	90.3%	66
WS_2@NiCoS	784.38	49.47	1212.30	93.23%	67
Z ZCS/GO/CN	811	33.3	624	81.08%	68
Co–Mn–S	537	73.52	10 200	90.03%	69
Zn–Co–S nanostrip	830	19.0	514	76%	70
Co–Zn–C–S	815	—	—	83.9%	71
Zn–Co bimetal sulfides	6.22 F cm^{-2}	0.124 mWh	21 mW cm^{-2}	68.4%	68
Nanostructured CoS	1056	31.4	200	90%	70
ZnS nanowires	781	51	200	87%	71
rGO/ZnCoS	891	29	2215	99%	68
DLS-optimized ZnS–CoS	1156	194	7260	93.87%	Our work

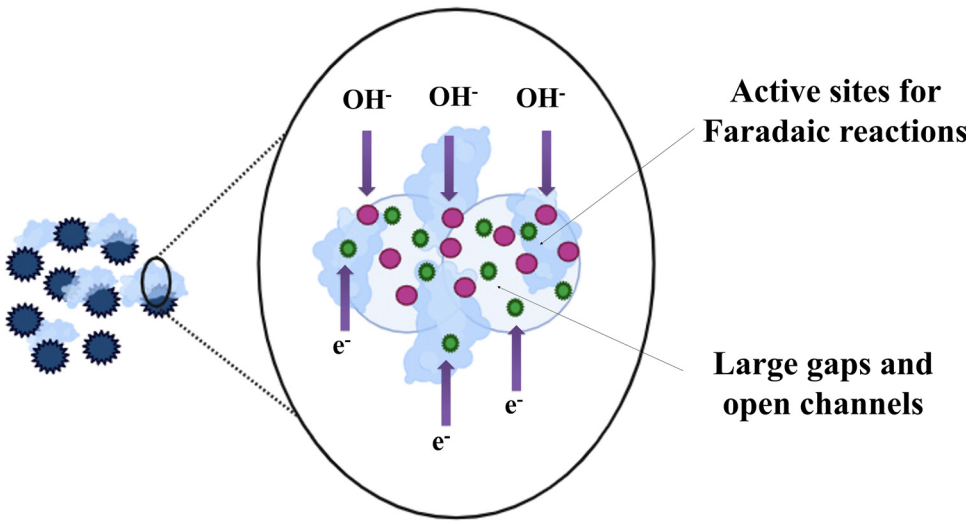

Scheme 1 Schematic illustration of the charge storage mechanism in optimized ZnS–CoS, showing abundant active sites for Faradaic reactions and large gaps/open channels that facilitate OH^- ion diffusion and electron transport, leading to enhanced electrochemical performance.

Table 5 HOMO and LUMO energies and bandgaps of ZnS, CoS, and ZnS–CoS NPs expressed in eV

Material	E_{HOMO} (eV)	E_{LUMO} (eV)	E_{L-H} gap (eV)
ZnS	−6.72039	−4.20143	2.51896
CoS	−11.6110	−8.85866	2.75234
ZnS–CoS	−10.8105	−8.28042	2.53008

after mixing, on the electronic structure and capacitive performance. Hence, ZnS–CoS achieves better electrochemical performance due to its improved conductivity, as predicted by computational calculations.

4.5 Machine learning models' performance

This study utilized Response Surface Methodology (RSM), Tree-based Pipeline Optimization Tool (TPOT), Artificial Neural Network (ANN), and stacking regressor models to accurately verify the experimental specific capacitance of ZnS. In the present study, potential window, current density, and scan rate were the input features, while specific capacitance was the output feature. The performance was evaluated on the basis of R^2 and RMSE metrics. The models were performed at different scan rates (5, 30, 60, 80, and 100 mV s^{-1}). For the stacking regressor model at different scan rates (5, 30, 60, 80, and 100 mV s^{-1}), MSE values of 0.002236, 0.002349, 0.002487, 0.002761, and 0.003014 were obtained, respectively, with corresponding R^2 values of 0.672140, 0.682545, 0.691387, 0.693611, and 0.695586, as shown in Fig. 13. It is clear from the figure that there is a slight increase in the R^2 values with an increase in the scan rate, which indicates that the model outstandingly performs at higher scan rates, and the best results are obtained at 100 mV s^{-1}. It might be due to the reason that at a faster scan rate, the models can process data points faster, leading to enhanced overall prediction time. The RSM performed the worst, with R^2 of 0.46, RMSE of 0.42, and MAE of 0.33 (Fig. S7). TPOT improved the fit, resulting in R^2 of

CoS	-11.6110	-8.85866	2.75234
ZnS-CoS	-10.8105	-8.28042	2.53008

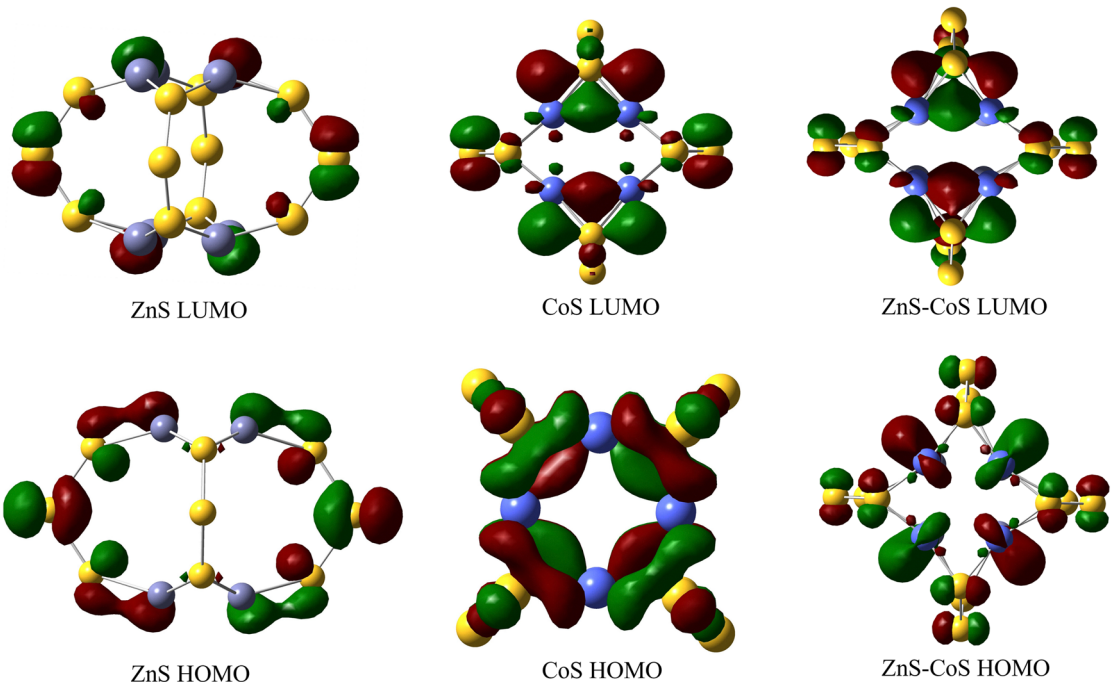

Fig. 11 Computationally derived HOMO–LUMO orbital distributions of ZnS, CoS, and ZnS–CoS nanoparticles, illustrating the electronic structure and frontier molecular orbitals responsible for their charge transfer behavior.

0.57 with RMSE of 0.36 and MAE of 0.28 (Fig. S8). ANN showed slight improvement with R^2 = 0.57, RMSE = 0.34, and MAE = 0.26 (Fig. S9), indicating its ability to handle nonlinear datasets. The stacking regressor had the highest predictive accuracy, with R^2 = 0.67, RMSE = 0.28, and MAE = 0.21 (Fig. 13). Overall, the ranking of model performance was stacking regressor > ANN > TPOT > RSM. These findings clearly show that the ensemble approach is the most reliable method for modeling the nonlinear capacitance behavior of the electrode system.

Furthermore, it is clear from the above discussion that the artificial neural network (ANN) performed better in terms of prediction than the RSM regression model. The accuracy of the ANN model is attributed to its flexibility in capturing nonlinear behavior,[75,76] which is well documented in the literature. For instance, Khoshraftar *et al.* used both RSM and an ANN to model CO_2 adsorption on Fe–Ni/AC-modified carbon nanotubes. The ANN model achieved R^2 = 0.9990 (MSE = 4.247 × 10^{-4}), whereas the RSM model had predicted R^2 = 0.8899.[77] In another study, Luan *et al.* optimized PVB synthesis using both RSM and ANN. Their results show RSM: R^2 = 0.9865, RMSE = 0.4754; *versus* ANN: R^2 = 0.9962, RMSE = 0.2551.[78] In short, ANN models frequently achieve superior predictive accuracy and robustness than RSM because they can fit the interacting nonlinear behavior more flexibly.

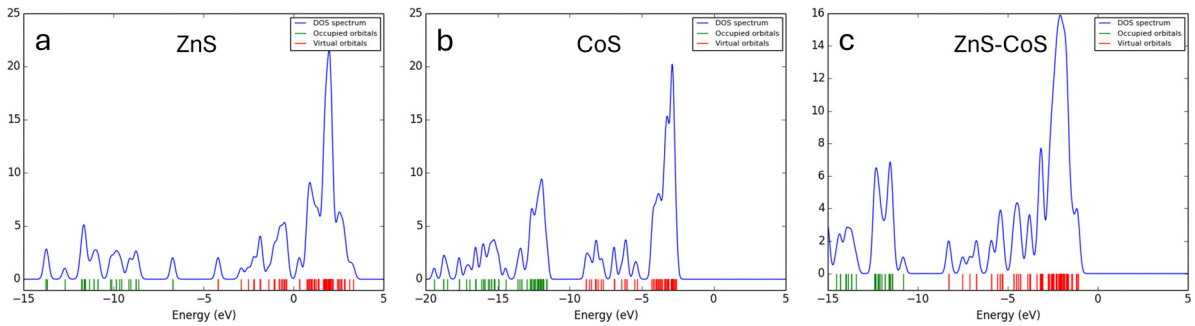

Fig. 12 Density of states (DOS) spectra of (a) ZnS, (b) CoS, and (c) ZnS–CoS nanoparticles, highlighting the electronic states near the Fermi level and their role in governing charge transport properties.

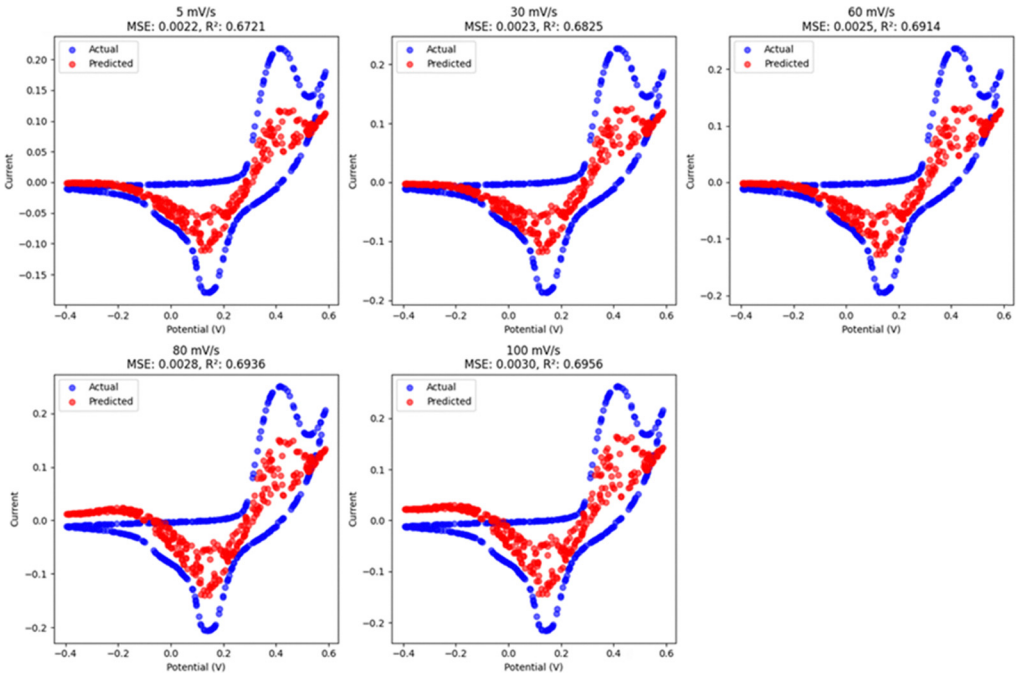

Fig. 13 Comparison between the experimental results and the stacking regressor model predictions at different scan rates.

Although extensive work has been reported on mixed transition metal sulfide nanoparticles, very limited attention has been paid to controlling their particle size and stability. Since parameters such as precursor concentration, pH, temperature, reagent addition rate, and stabilizer concentration[28,29] directly influence the size, shape, and surface chemistry, their optimization is essential for tuning the electrochemical performance. Previous studies have suggested that the particle size and morphology control[36] can significantly enhance the properties of TMS-based electrodes; however, systematic strategies for improving specific capacitance, power density, and energy density remain lacking. In this work, we addressed this gap by optimizing key synthesis parameters to achieve controlled nanoparticle characteristics. The improved size and morphology directly contributed to enhanced electrochemical performance, demonstrating the importance of controlled synthesis in advancing TMS-based energy storage materials. For instance, Muhammad Sufyan Javed *et al.* reported a specific capacitance of 110 F g^{-1} for ZnS@$FeSe_2$ nanostructures,[79] A. Shah *et al.* achieved 95 F g^{-1} for ZnS/$CuSe_2$//AC,[80] while Hongxia Wang *et al.* reported 200 F g^{-1} for $Cu_5Sn_2S_7$/ZnS.[81] These earlier studies did not involve the optimization of nanoparticle characteristics. In contrast, our optimized nanoparticles achieved a much higher capacitance of 1156 F g^{-1}, along with improved power density and energy density (Table 4), demonstrating that careful optimization of synthesis parameters is a highly effective strategy for advancing the performance of TMS-based energy storage materials.

In addition, our study introduces novelty by predicting the specific capacitance of ZnS by using machine learning models, for the first time, at different scan rates, which has not been reported before. Unlike conventional ML approaches that face issues like overfitting and poor interpretability, we applied linearized data with advanced ML to achieve more robust and reliable predictions. Furthermore, DFT calculations revealed a reduced band gap in Zn–CO–S, which is directly correlated with enhanced electrochemical properties, thereby reinforcing the experimental outcomes.

5. Conclusion

In this study, we have successfully synthesized and optimized zinc cobalt sulfide (ZnS–CoS) nanoparticles by a co-precipitation method, followed by an in-depth optimization process using dynamic light scattering (DLS). The optimization was systematically carried out by varying crucial synthesis parameters including temperature, pH, reagent addition rate, and stabilizer concentration, to achieve well-dispersed, stable nanoparticles with controlled size and morphology. The influence of these parameters on hydrodynamic size, polydispersity index (PDI), zeta potential, and overall electrochemical properties was carefully analyzed. The optimized ZnS–CoS nanoparticles exhibited remarkable electrochemical performance, achieving an exceptional specific capacitance of 1156 F g^{-1} at 2 A g^{-1}, which is significantly higher than that of the individual ZnS and CoS electrodes. Furthermore, the energy density and power density were found to be 194 Wh kg^{-1} and 7260 W kg^{-1}, respectively, demonstrating a substantial enhancement over conventional transition metal sulfide-based electrodes. The electrochemical impedance spectroscopy (EIS) results confirmed a lower charge transfer resistance (35.88 Ω), which facilitated faster ion transport and improved electrical conductivity. Additionally, galvanostatic charge–discharge (GCD)

analysis indicated excellent rate capability and high capacitance retention, with the optimized ZnS–CoS electrode maintaining 93.87% of its initial capacitance after 10 000 continuous charge–discharge cycles. This highlights its superior stability and durability, making it a highly promising material for long-term energy storage applications. To further understand the charge storage mechanism, Dunn's power law model was applied, revealing that the ZnS–CoS electrode exhibited a dominant surface-controlled capacitive contribution of 52.30% at a scan rate of 5 mV s^{-1}, further supporting its excellent charge storage capability. Computational calculations, including density of states (DOS) and HOMO–LUMO energy gap analysis, confirmed the synergistic effect of Zn and Co, resulting in enhanced electronic conductivity and improved charge transport properties. Stacking regressor, TPOT, ANN, and RSM models were applied to verify the experimental specific capacitance of ZnS. The performance metrics of these models follow the ranking of stacking regressor > ANN > TPOT > RSM. This study demonstrates how well the stacking regression model can be used to improve the electrical and electrochemical behavior.

Overall, this study demonstrated that precise nanoparticle size and morphology optimization using DLS play a crucial role in enhancing the electrochemical performance of ZnS–CoS electrodes. The optimized ZnS–CoS nanoparticles not only surpass many previously reported transition metal sulfide-based electrodes but also establish a new benchmark for next-generation supercapacitor materials. The combination of high capacitance, superior energy and power density, excellent stability, and favorable charge storage kinetics makes ZnS–CoS a highly promising candidate for high-performance energy storage devices. Future research can explore further material modifications, hybrid structures, and scalable synthesis approaches to enable the widespread adoption of ZnS–CoS for commercial supercapacitor applications.

Author contributions

Hafeez Ur Rehman: Benchwork, characterization, and initial draft preparation. Hamza Khan: computational analysis, reviewing and editing. Zeeshan Abbasi and Amir Waseem: characterization. Lotfi Ben Tahar: funding and reviewing. Rafaqat Ali Khan: electrochemical analysis. Ahson Jabbar Shaikh: conceptualization, visualization, methodology, investigation, supervision, writing, reviewing, editing, and validation. All authors read and approved the final manuscript.

Conflicts of interest

The authors declare that they have no competing interests.

Data availability

The data supporting this article have been included as part of the SI. Supplementary information contains the synthesis and characterization of ZnS and CoS nanoparticles, temperature-based optimization, pH-based optimization, optimization based on reagent addition time, and stabilizer concentration-based optimization. It also includes comparison between experimental results and RSM, TPOT, and ANN model predictions at different scan rates. See DOI: **https://doi.org/10.1039/d5ma00846h**.

Acknowledgements

The authors extend their appreciation to the Deanship of Scientific Research at Northern Border University, Arar, KSA, for funding this research work through the project number ''NBU-FFR-2025-2482-04''.

References

1 A. H. Alami, *Mechanical energy storage for renewable and sustainable energy resources*, Springer, 2020.
2 A. G. Olabi, *et al.*, Critical review of energy storage systems, *Energy*, 2021, **214**, 118987.
3 Y. Gao and L. Zhao, Review on recent advances in nanostructured transition-metal–sulfide-based electrode materials for cathode materials of asymmetric supercapacitors, *Chem. Eng. J.*, 2022, **430**, 132745.
4 S. A. Ahmad, *et al.*, $CoSe_2$@ZnS microsphere arrays with remarkable electrochemical performance for hybrid asymmetric supercapacitor, *J. Energy Storage*, 2023, **73**, 109090.
5 R. Barik and P. P. Ingole, Challenges and prospects of metal sulfide materials for supercapacitors, *Curr. Opin. Electrochem.*, 2020, **21**, 327–334.
6 H. Khan, *et al.*, Tailoring hydrodynamic size and stability of TiO_2–SiO_2 nanoparticles for enhanced electrochemical performance of supercapacitors, *Mater. Chem. Phys.*, 2026, **347**, 131423.
7 M. Z. Iqbal, M. M. Faisal and S. R. Ali, Integration of supercapacitors and batteries towards high-performance hybrid energy storage devices, *Int. J. Energy Res.*, 2021, **45**(2), 1449–1479.
8 X. Rui, H. Tan and Q. Yan, Nanostructured metal sulfides for energy storage, *Nanoscale*, 2014, **6**(17), 9889–9924.
9 H. Rashid Khan and A. Latif Ahmad, Supercapacitors: Overcoming current limitations and charting the course for next-generation energy storage, *J. Ind. Eng. Chem.*, 2025, **141**, 46–66.
10 A. Das, *et al.*, Performance and future directions of transition metal sulfide-based electrode materials towards supercapacitor/supercapattery, *WIREs Energy Environ.*, 2022, **11**(1), e414.
11 P. Pazhamalai, *et al.*, Copper tungsten sulfide anchored on Ni-foam as a high-performance binder free negative electrode for asymmetric supercapacitor, *Chem. Eng. J.*, 2019, **359**, 409–418.

12 I. Hussain, *et al.*, Different controlled nanostructures of Mn-doped ZnS for high-performance supercapacitor applications, *J. Energy Storage*, 2020, **32**, 101767.
13 Y. Gan, *et al.*, Trumpet-Like ZnS@C Composite for High-Performance Potassium Ion Battery Anode, *Chem. – Eur. J.*, 2023, **29**(32), e202300373.
14 Z. Li, *et al.*, Flaky CoS_2 and graphene nanocomposite anode materials for sodium-ion batteries with improved performance, *RSC Adv.*, 2016, **6**(74), 70632–70637.
15 T. Ma, *et al.*, Nickel-cobalt-molybdenum sulfides with adjustable morphology via coprecipitation and hydrothermal conversion as high-performance electrodes for asymmetric supercapacitors, *J. Alloys Compd.*, 2020, **838**, 155631.
16 S. Venkateshalu, D. Rangappa and A. N. Grace, Hydrothermal synthesis and electrochemical properties of CoS_2–reduced graphene oxide nanocomposite for supercapacitor application, *Int. J. Nanosci.*, 2018, **17**(01–02), 1760020.
17 W. Chen, C. Xia and H. N. Alshareef, One-step electrodeposited nickel cobalt sulfide nanosheet arrays for high-performance asymmetric supercapacitors, *ACS Nano*, 2014, **8**(9), 9531–9541.
18 M.-R. Gao, *et al.*, Nanostructured metal chalcogenides: synthesis, modification, and applications in energy conversion and storage devices, *Chem. Soc. Rev.*, 2013, **42**(7), 2986–3017.
19 Y. Liu, *et al.*, Design, synthesis, and energy-related applications of metal sulfides, *Mater. Horiz.*, 2016, **3**(5), 402–421.
20 H. Li, *et al.*, Zinc cobalt sulfide nanoparticles as high performance electrode material for asymmetric supercapacitor, *Electrochim. Acta*, 2019, **319**, 716–726.
21 N. Du, *et al.*, Nanosheet-assembled NiS hollow structures with double shells and controlled shapes for high-performance supercapacitors, *Chem. Eng. J.*, 2017, **323**, 415–424.
22 S. Shafaat, *et al.*, Understanding adsorption phenomena through dynamic light scattering and stability measurements, *Int. J. Environ. Anal. Chem.*, 2025, 1–22.
23 M. Y. Afzal, *et al.*, Understanding Photocatalytic Degradation of RB5 Dye under Salts Using Nickel Sulfide Nanoparticles: Insights from Dynamic Light Scattering and Theoretical Investigations, *ACS Omega*, 2025, **10**(30), 32918–32938.
24 H. Li, *et al.*, Electrochemical performance of $LiNi_{0.5}Mn_{0.5}O_2$ with different synthesis methods, *Rare Met.*, 2015, **34**, 580–585.
25 H. Dong, A. Wang and G. M. Koenig Jr, Role of coprecipitation and calcination of precursors on phase homogeneity and electrochemical properties of battery active materials, *Powder Technol.*, 2018, **335**, 137–146.
26 M. Valenzuela, *et al.*, Comparison between sol-gel, coprecipitation and wet mixing synthesis of $ZnAl_2O_4$, *J. Sol-Gel Sci. Technol.*, 1997, **8**(1), 107–110.
27 R. Rai, S. Alwani and I. Badea, Polymeric nanoparticles in gene therapy: new avenues of design and optimization for delivery applications, *Polymers*, 2019, **11**(4), 745.
28 K. Do Kim, *et al.*, Optimization of parameters for the synthesis of zinc oxide nanoparticles by Taguchi robust design method, *Colloids Surf., A*, 2007, **311**(1–3), 170–173.
29 K. Nemade and S. Waghuley, Ultra-violet C absorption and LPG sensing study of zinc sulphide nanoparticles deposited by a flame-assisted spray pyrolysis method, *J. Taibah Univ. Sci.*, 2016, **10**(3), 437–441.
30 A. Saleem, *et al.*, The synergistic effect of electron lone pairs and aromaticity on the binding affinity towards metal surfaces, *Colloids Surf., A*, 2023, **664**, 131127.
31 J. Xu, *et al.*, One-step electrodeposition fabrication of Ni_3S_2 nanosheet arrays on Ni foam as an advanced electrode for asymmetric supercapacitors, *Sci. China Mater.*, 2019, **62**(5), 699–710.
32 W. Saeed, *et al.*, Interactive behavior of graphene quantum dots towards noble metal surfaces, *Phys. E*, 2023, **147**, 115596.
33 G. Huang, F. Huang and W. Dong, Machine learning in energy storage material discovery and performance prediction, *Chem. Eng. J.*, 2024, 152294.
34 Z. Lu, Computational discovery of energy materials in the era of big data and machine learning: a critical review, *Mater. Rep.: Energy*, 2021, **1**(3), 100047.
35 W. Z. Tawfik, *et al.*, An artificial neural network model for capacitance prediction of porous carbon-based supercapacitor electrodes, *J. Energy Storage*, 2023, **73**, 108830.
36 X. Lu, *et al.*, Research on prediction of energy density and power density of biomass carbon-based supercapacitors based on machine learning, *Sustainable Mater. Technol.*, 2025, **44**, e01309.
37 C. Liu, Q. Li and K. Wang, State-of-charge estimation and remaining useful life prediction of supercapacitors, *Renewable Sustainable Energy Rev.*, 2021, **150**, 111408.
38 A. J. Shaikh, *et al.*, Plasmonic Effects, Size and Biological Activity Relationship of Au–Ag Alloy Nanoparticles, *J. Nano Res.*, 2018, **54**, 98–111.
39 M. Ullah, *et al.*, Sustainable graphitic carbon derived from oil palm frond biomass for supercapacitor application: effect of redox additive and artificial neural network-based modeling approach, *J. Electroanal. Chem.*, 2024, **971**, 118570.
40 W. Z. Tawfik, *et al.*, Insights into the specific capacitance of CNT-based supercapacitor electrodes using artificial intelligence, *RSC Adv.*, 2025, **15**(5), 3155–3167.
41 B. Reddy, *et al.*, Modeling capacitance of carbon-based supercapacitors by artificial neural networks, *J. Energy Storage*, 2023, **72**, 108537.
42 M. A. Ebied, M. A. Azim and A. Emad-Eldeen, AI-based approach for predicting the storage performance of zinc oxide-based supercapacitor electrodes, *J. Energy Storage*, 2024, **94**, 112292.
43 T. Dongale, *et al.*, Development of nano fiber MnO_2 thin film electrode and cyclic voltammetry behavior modeling using artificial neural network for supercapacitor application, *Mater. Sci. Semicond. Process*, 2015, **36**, 43–48.
44 P. Liu, *et al.*, New insights into the performance of biomass carbon-based supercapacitors based on interpretable machine learning approach, *J. Energy Storage*, 2025, **118**, 116300.

45 R. Bu, *et al.*, ''One-for-two'' strategy: the construction of high performance positive and negative electrode materials via one Co-based metal organic framework precursor for boosted hybrid supercapacitor energy density, *J. Power Sources*, 2022, **541**, 231689.
46 J. Zhang, *et al.*, Chemically coupled 0D-3D hetero-structure of Co_9S_8–Ni_3S_4 hollow spheres for Zn-based supercapacitors, *Chem. Eng. J.*, 2022, **430**, 132836.
47 S. Bhattacharjee, DLS and zeta potential–what they are and what they are not?, *J. Controlled Release*, 2016, **235**, 337–351.
48 M. Kasture, *et al.*, Synthesis of silver nanoparticles by sophorolipids: effect of temperature and sophorolipid structure on the size of particles, *J. Chem. Sci.*, 2008, **120**, 515–520.
49 B. Diwakar, *et al.*, Carboxymethyl cellouse stabilized cobalt sulfide nanoparticles: preparation, characterization and application, *J. Cluster Sci.*, 2023, **34**(5), 2429–2439.
50 D. Amir, *et al.*, Effect of Stabilizers in the Synthesis of Silver Nanoparticles and Methylene Blue Oxidation, *IOP Conference Series: Materials Science and Engineering*, IOP Publishing, 2021.
51 Y. V. de Santana, *et al.*, Experimental and theoretical studies on the enhanced photoluminescence activity of zinc sulfide with a capping agent, *J. Appl. Phys.*, 2011, **110**(12), 123507.
52 U. Senapati and D. Sarkar, Synthesis and characterization of biopolymer protected zinc sulphide nanoparticles, *Superlattices Microstruct.*, 2015, **85**, 722–733.
53 M. B. Muradov, *et al.*, Synthesis and characterization of cobalt sulfide nanoparticles by sonochemical method, *Infrared Phys. Technol.*, 2018, **89**, 255–262.
54 T. Abza, *et al.*, Characterization of cobalt sulfide thin films synthesized from acidic chemical baths, *Adv. Mater. Sci. Eng.*, 2020, **2020**(1), 2628706.
55 A. Ait-karra, *et al.*, Effect of hydrothermal temperature on the structural, morphological, optical properties and photocatalytic performances of cobalt sulfide nanomaterials, *J. Alloys Compd.*, 2024, **999**, 174946.
56 Y. Zhang, *et al.*, Coupling of heterogeneous advanced oxidation processes and photocatalysis in efficient degradation of tetracycline hydrochloride by Fe-based MOFs: synergistic effect and degradation pathway, *Chem. Eng. J.*, 2019, **369**, 745–757.
57 R. Ramachandran, *et al.*, Synthesis of cobalt sulfide–graphene (CoS/G) nanocomposites for supercapacitor applications, *IEEE Trans. Nanotechnol.*, 2013, **12**(6), 985–990.
58 J. Aftab, *et al.*, Synergetic electrochemical performance of tungsten oxide/tungsten disulfide/MWCNTs for high-performance aqueous asymmetric supercapattery devices, *J. Alloys Compd.*, 2023, **965**, 171366.
59 J. Zhao, *et al.*, Multilayer dodecahedrons Zn-Co sulfide for supercapacitors, *Electrochim. Acta*, 2020, **354**, 136714.
60 M. Imran, *et al.*, Designing of WS_2@NiCoS@ ZnS nanocomposite electrode material for high-performance energy storage applications, *Crystals*, 2024, **14**(11), 916.
61 D. Ravisankar, *et al.*, Novel Surface-Enriched Spiky Ball With Spines $NiCo_2S_4$@GO/CNT Electrode Material for a High-Performance Flexible Asymmetric Supercapacitor, *ECS J. Solid State Sci. Technol.*, 2024, **13**(1), 011001.
62 L. A. Miya, *et al.*, Eco-friendly and sustainable supercapacitor design: cobalt sulfide nanoparticles embedded on carbon cloth as an electrode material for asymmetric devices, *Chem. Pap.*, 2025, 1–15.
63 K. Ashok Kumar, *et al.*, Effect of bi-functional hierarchical flower-like CoS nanostructure on its interfacial charge transport kinetics, magnetic and electrochemical behaviors for supercapacitor and DSSC applications, *Sci. Rep.*, 2019, **9**(1), 1228.
64 W. Zhou, *et al.*, CoS_x/C hierarchical hollow nanocages from a metal–organic framework as a positive electrode with enhancing performance for aqueous supercapacitors, *RSC Adv.*, 2019, **9**(20), 11253–11262.
65 S. Zainab, *et al.*, Exploring electrolyte specific effects on multisheets 2-dimensional $Ti_3C_2T_x$–$BiFeO_3$ nanocomposites electrodes for high-performance supercapacitors applications, *Sci. Rep.*, 2025, **15**(1), 22848.
66 M. Z. Iqbal, U. Abbasi and M. Alzaid, Cobalt manganese phosphate and sulfide electrode materials for potential applications of battery-supercapacitor hybrid devices, *J. Energy Storage*, 2022, **50**, 104632.
67 S. Vijayakumar, *et al.*, Facile synthesis of Zn–Co–S nanostrip cluster arrays on Ni foam for high-performance hybrid supercapacitors, *Nanomaterials*, 2021, **11**(12), 3209.
68 R. Ahmad, *et al.*, Zeolitic imidazolate frameworks derived Co–Zn-nanoporous carbon-sulfide material for supercapacitors, *Electrochim. Acta*, 2022, **404**, 139739.
69 X. Zang, *et al.*, Solvent-Controlled Morphology of Zinc–Cobalt Bimetallic Sulfides for Supercapacitors, *Molecules*, 2023, **28**(18), 6578.
70 R. Rakhi, *et al.*, Nanostructured cobalt sulfide-on-fiber with tunable morphology as electrodes for asymmetric hybrid supercapacitors, *J. Mater. Chem. A*, 2014, **2**(38), 16190–16198.
71 M. Rauf, *et al.*, Facile hydrothermal synthesis of zinc sulfide nanowires for high-performance asymmetric supercapacitor, *J. Saudi Chem. Soc.*, 2022, **26**(4), 101514.
72 P. De, *et al.*, Role of porosity and diffusion coefficient in porous electrode used in supercapacitors–Correlating theoretical and experimental studies, *Electrochem. Sci. Adv.*, 2023, **3**(1), e2100159.
73 A. M. Afzal, *et al.*, Exploring the redox characteristics of porous ZnCoS@ rGO grown on nickel foam as a high-performance electrode for energy storage applications, *RSC Adv.*, 2023, **13**(31), 21236–21248.
74 Y. Gao, *et al.*, Double metal ions synergistic effect in hierarchical multiple sulfide microflowers for enhanced supercapacitor performance, *ACS Appl. Mater. Interfaces*, 2015, **7**(7), 4311–4319.
75 T. Li, *et al.*, Predicting high-strength concrete's compressive strength: a comparative study of artificial neural networks, adaptive neuro-fuzzy inference system, and response surface methodology, *Materials*, 2024, **17**(18), 4533.
76 Y. M. Desalegn, *et al.*, RSM versus ANN for modeling and optimization of magnetic adsorbent based on montmorillonite and $CoFe_2O_4$, *Appl. Water Sci.*, 2024, **14**(6), 129.

77 Z. Khoshraftar, A. Ghaemi and A. Hemmati, Comprehensive investigation of isotherm, RSM, and ANN modeling of CO_2 capture by multi-walled carbon nanotube, *Sci. Rep.*, 2024, **14**(1), 5130.
78 W. Luan, *et al.*, Optimization of a polyvinyl butyral synthesis process based on response surface methodology and artificial neural network, *RSC Adv.*, 2023, **13**(11), 7682–7693.
79 S. A. Ahmad, *et al.*, Facile synthesis of hierarchical ZnS@$FeSe_2$ nanostructures as new energy-efficient cathode material for advanced asymmetric supercapacitors, *J. Sci.:Adv. Mater. Devices*, 2022, **7**(4), 100489.
80 S. A. Ahmad, *et al.*, High power aqueous hybrid asymmetric supercapacitor based on zero-dimensional ZnS nanoparticles with two-dimensional nanoflakes $CuSe_2$ nanostructures, *Ceram. Int.*, 2023, **49**(12), 20007–20016.
81 F. Yu, *et al.*, Flower-like $Cu_5Sn_2S_7$/ZnS nanocomposite for high performance supercapacitor, *Chin. Chem. Lett.*, 2019, **30**(5), 1115–1120.